

Praful Gupta,¹ Jack L. Glover,² Nicholas G. Paulter, Jr.,² and Alan C. Bovik³

Studying the Statistics of Natural X-ray Pictures

Reference

Gupta, P., Glover, J. L., Paulter, N. G., Jr., and Bovik, A. C., "Studying the Statistics of Natural X-ray Pictures," *Journal of Testing and Evaluation*, Vol. 46, No. 4, 2018, pp. 1478–1488, <https://doi.org/10.1520/JTE20170345>. ISSN 0090-3973

ABSTRACT

In this article, we have studied and analyzed the statistics of both pristine and distorted bandpass X-ray images. In the past, we have shown that the statistics of natural, bandpass-filtered visible light (VL) pictures, commonly expressed by natural scene statistic (NSS) models, can be used to create remarkably powerful, perceptually relevant predictors of perceptual picture quality. We find that similar models can be developed that apply quite well to X-ray image data. We have also studied the potential of applying these statistical X-ray NSS models to the design of algorithms for automatic image quality prediction of X-ray images, such as might occur in security, medicine, and material inspection applications. As a demonstration of the discrimination power of these models, we devised an application of NSS models to an image modality classification task, whereby VL, X-ray, infrared, and millimeter-wave images can be effectively and automatically distinguished. Our study is conducted on a dataset of X-ray images made available by the National Institute of Standards and Technology.

Keywords

natural scene statistic, X-ray images, modality classification, National Institute of Standards and Technology

Introduction

X-ray images are widely used in industrial nondestructive material testing [1], archeological photography [2], food inspection [3], medical imaging [4,5], security screening [6], and many other fields. In particular, X-ray security systems are extensively used for airport security screening where they are implemented for object or material recognition and inspection in a variety of modes, including single- or dual-energy systems, single- or dual-view systems, scattering systems, tomographic systems, and stereo matching dual-view systems (for 3-D) [6]. The technology of X-ray Computed Tomography (CT) that is extensively used in medical imaging has also become an important component of aviation security screening systems, which are used to conduct efficient and nondestructive inspection of baggage and other objects [6–8]. Other multi-sensor X-ray systems that use data fusion techniques of combining different modes also exist [7].

There are a number of image-quality measurements that are used to characterize the performance of portable X-ray imagers and which define standard Image Quality Indicators (IQIs). These include spatial resolution, useful penetration, organic material detection, dynamic range, measured noise, flatness

Manuscript received June 14, 2017; accepted for publication March 28, 2018; published online May 14, 2018.

¹ Department of Electrical and Computer Engineering, The University of Texas at Austin, 2501 Speedway, Austin, TX 78712, USA (Corresponding author), e-mail: praful_gupta@utexas.edu, <https://orcid.org/0000-0001-7520-3572>

² National Institute of Standards and Technology, 100 Bureau Dr., Gaithersburg, MD 20899, USA, <https://orcid.org/0000-0001-5656-5228> (J.L.G.), <https://orcid.org/0000-0002-9782-0894> (N.G.P.)

³ Department of Electrical and Computer Engineering, The University of Texas at Austin, 2501 Speedway, Austin, TX 78712, USA

of field, image extent, and subjective quality (using human judgment) [9,10]. The development of these methods and quality standards reflect the significant efforts that have been made toward developing numerical performance metrics for X-ray imaging systems. Chen, Pan, and Han developed a No-Reference X-ray Image Quality Evaluation method that controls the dose of X-ray radiation based on the weighted entropy of the grayscale distribution of an image [11]. Bolfing, Halbherr, and Schwaninger applied statistical approaches to examine various image-based factors, such as view difficulty, superposition, and bag complexity, that can significantly affect threat detection performance in aviation X-ray security screening systems [12]. Although X-ray images have been extensively studied, little work has been done to solve the important problem of perceptual assessment of X-ray imager quality, or analyzing existing standard IQIs in light of perceptual principles that could help explain how images produced by X-ray imagers impact human and automatic image interpretation tasks in many applications, including security and medical imaging.

The main goal of this work is to develop Natural Scene Statistic (NSS) models of X-ray images and to explore their possible efficacy as tools for assessing X-ray image quality and its effect on visual task performance. NSS models have been demonstrated to successfully capture the statistical consistencies of natural images both in the spatial [13] and wavelet domains [14]. Here, a natural image is one formed by sensing radiation projected from interactions with the real world, including both man-made and naturally occurring objects, but excluding computer-generated images. Examples of NSS models include the $1/f$ model of the amplitude spectrum of visible light (VL) images, sparse coding characteristics of cortical-like filters [15], and the underlying gaussianity of perceptually processed band-pass images [16]. Because cortical processing in mammalian visual systems has adapted to natural visual stimuli, the statistical properties of the real-world environment are quite relevant to the design of visual interpretation algorithms [17,18].

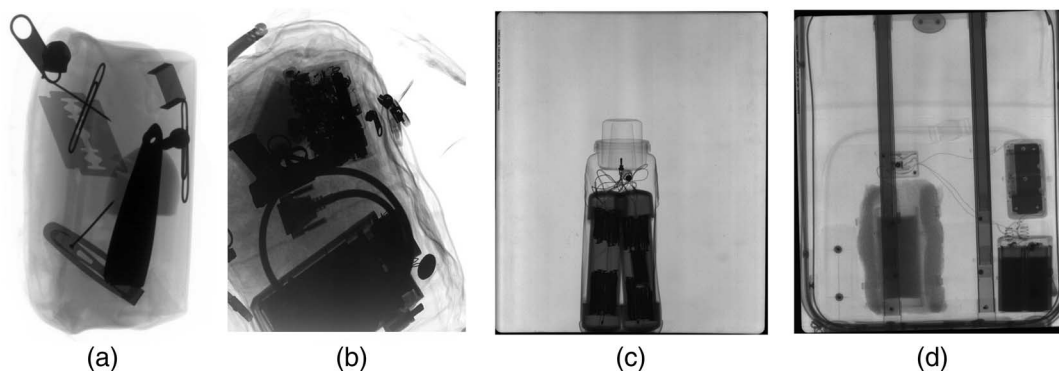
Given the remarkable success of NSS models of photographic VL images and of perceptual quality models based on them [13,14,19,20], it is of interest to also model the statistics of natural images from other modalities. Long-wave infrared (LWIR) images, such as those captured by thermal cameras, possess a similar degree of statistical consistency as VL images [21]. NSS models of LWIR images have proven quite useful for a variety of visual tasks, such as IR image quality prediction, VL and IR image discrimination, analysis of IR-specific distortions (such as the halo effect), and thermal nonuniformities. More recently, the statistics of fused LWIR and VL images were analyzed, and a NSS-based algorithm for fused image quality assessment (IQA) was developed [22]. With this motivation, we seek to understand and model the NSS of X-ray images toward improving the solutions to many X-ray imaging problems.

Since the image modality provides important information about the visual characteristics of an image, distinguishing images based on modality is a fundamental preprocessing step in various image retrieval processes. In medical image retrieval, text-based approaches relying on annotation or caption identification and content-based image retrieval systems are commonly used to distinguish images from different medical domains, including radiographs, brain magnetic resonance images, mammograms, and lung CTs [23,24]. In this article, we study the scene statistics of undistorted and distorted X-ray pictures, demonstrating the effectiveness of perceptually powerful NSS descriptors in discriminating images from various modalities.

DISTORTION MODELS

We applied two levels of distortion each of blur and noise to a set of randomly selected pristine images from the National Institute of Standards and Technology (NIST) and GDXray [25] databases. A few examples of these X-ray images are shown in Fig. 1. Here we describe the generative noise models that we used to distort the X-ray images. It is well established that photon-counting noise in X-ray images is realistically modeled as a Poisson process, where

FIG. 1 (a) and (b) are examples of X-ray images from GDXray, and (c) and (d) are images from the National Institute of Standards and Technology databases. The GDXray database contains 8-bit grayscale X-ray images, while the NIST images are 16-bit.



the probability distribution of the number of incident photons [26], N , is given by the following:

$$Pr(N = k) = \frac{e^{-\lambda}(\lambda)^k}{k!} \quad (1)$$

where λ is the expected number of photons measured by the sensor. Thus, varying the number of incident photons⁴ can be effectively utilized to introduce a desired level of noise in the images. In order to simulate the appropriate number of incident photons, it is essential to have a mechanism to relate image grayscale units to detected photon counts. Ideally, the relationship between the number of detected photons, n , and the image grayscale value, i , at the pixel of interest is linear [27], as shown in the following equation:

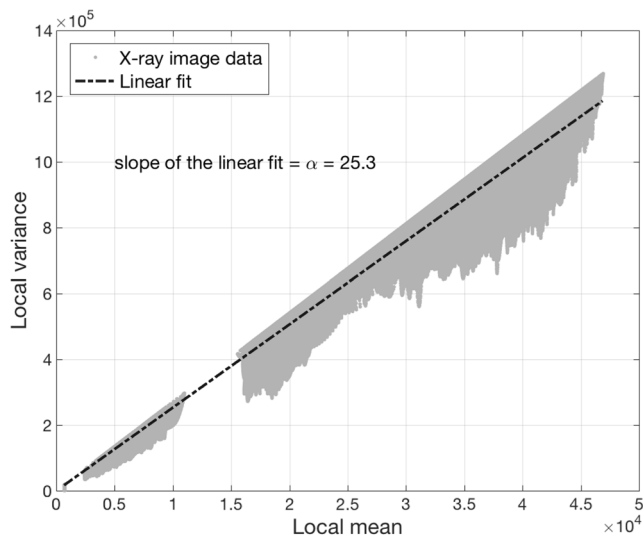
$$i = \alpha \cdot n \quad (2)$$

where α is the gain of the imaging device. Since the detected photon count follows Poisson statistics, the pixel variance, $Var(i)$, increases linearly with the pixel mean \bar{i} that is given as follows [28]:

$$\frac{Var(i)}{\bar{i}} = \frac{\alpha^2 \cdot Var(n)}{\alpha \cdot \bar{n}} = \alpha \quad (3)$$

The gain α is computed using 25 % of the total pixels that have the least variance to mean ratio (VMR), to avoid variance contribution from the object being imaged. Fig. 2 depicts the linear relationship between the local variance and local mean of an X-ray image, indicating the effective point-to-point modeling of photon-counting noise by Poisson statistics.

FIG. 2 Plot between the local variance and local mean of X-ray image pixels that correspond to the lowest 25 % of VMR regions. A good linear fit to the image data suggests that photon counting noise can be well modeled by Poisson statistics.



Having computed the gain, α , the effective number of detected photons for each pixel is computed using Eq 2. To apply different levels of noise to the image, a multiplicative factor, k , is used to simulate the effect of the reduced number of detected photons, $n_{eff} = n/k$. For most practical purposes, photon noise can be approximately modeled by a Gaussian distribution whose mean and variance depends on the detected photon count [29,30] as given by the following:

$$n_{noisy} = \mathcal{N}(n_{eff}, n_{eff} + \eta), \quad (4)$$

where $\eta = 1$ is the variance of noise that is due to other factors, including sensor-based sources of noise, e.g., read noise. Finally, a noisy grayscale image is computed from the noisy photon field, n_{noisy} , at each location on the image plane using Eq 2.

Two levels of blur were also generated using a Gaussian blur kernel with scale parameter $\sigma_b = \{16, 32\}$ pixels. Sample images from each distortion category (most severe distortion level) are illustrated in Fig. 3.

NSS of X-ray Images

In a highly groundbreaking study of the statistics of VL images, Ruderman observed that preprocessing natural images by a local linear bandpass operation followed by a divisive nonlinearity (energy normalization) has a decorrelating and Gaussianizing effect [16]. This property of natural images has been used to capture the severity of perceptual image distortion in a number of highly successful Image Quality Assessment (IQA) models and algorithms [13,20,31,32]. Here, we study this process when applied to X-ray images. Given an input intensity image, I , define:

$$\hat{I}(i,j) = \frac{I(i,j) - \mu(i,j)}{\sigma(i,j) + c} \quad (5)$$

where $i \in \{1, 2, \dots, M\}$, $j \in \{1, 2, \dots, N\}$ are spatial indexes, M and N are the image height and width, respectively, and $c = 1$ is a constant that stabilizes computation when the denominator is small. The resulting values \hat{I} are usually referred to as Mean Subtracted Contrast Normalized (MSCN) coefficients. Assuming that the MSCN coefficients follow a Gaussian distribution, the weighted sample estimates of the local image mean μ and standard deviation σ are given by the following equations:

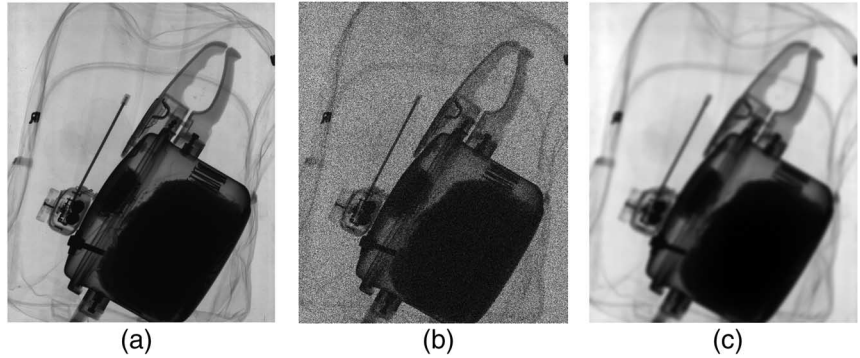
$$\mu(i,j) = \sum_{k=-K}^K \sum_{l=-L}^L w_{k,l} I_{k,l}(i,j) \quad (6)$$

$$\sigma(i,j) = \sqrt{\sum_{k=-K}^K \sum_{l=-L}^L w_{k,l} (I_{k,l}(i,j) - \mu(i,j))^2} \quad (7)$$

⁴We assume the efficiency of the detector of imaging system to be 1 so that the number of incident photons is equal to the number of detected photons.

FIG. 3

(a) Gaussian blur applied to the original pristine image, and the X-ray images in (b) and (c) depict severe distortion levels of multiplicative noise.



where $w = \{w_{k,l} | k = -K, \dots, K \text{ and } l = -L, \dots, L\}$ is a 2-D circularly symmetric Gaussian weighting function normalized to have unit volume. We use $K = L = 7$.

As shown in **Fig. 4a**, the histograms of MSCN coefficients of natural X-ray images exhibit a Gaussian-like appearance very similar to those of VL images. The scale invariant behavior of MSCN coefficients suggests that X-ray images, like VL images, are naturally multiscale, i.e., they show statistically consistent behavior across multiple scales. This demonstrates that undistorted X-ray images also possess a characteristic statistical regularity regardless of contents when free of noticeable distortions. We introduced two levels of distortion of blur and noise on the X-ray images. These distortions perturb the statistics of MSCN coefficients in a characteristic manner, as shown in **Fig. 4b**. Blur introduces a higher degree of correlation between neighboring pixels, resulting in thinner MSCN histograms (more Laplacian-like), while added noise produces random variations in the image, producing wider histograms. As demonstrated in **Fig. 4b** and **c**, these changes become more prominent in higher levels of distortion. Since these distortions modify the histogram in a characteristic manner, it becomes possible to predict the type and severity of distortion afflicting an image.

We use a parametrized zero-mean Generalized Gaussian Distribution (GGD) to model the MSCN coefficients of both pristine and distorted X-ray images. We estimate two parameters (α, σ_{ggd}^2) from each image, which are obtained from the GGD fit to the MSCN coefficients, where α is the shape parameter, while σ_{ggd}^2 determines the variance of the distribution. A formal definition of the GGD, along with a detailed explanation of the moment matching approach [33] used to estimate its parameters, is given in **Appendix A**. The feature tuple, (α, σ_{ggd}^2) , is denoted by f in **Table 1**.

The statistics of products of spatially adjacent bandpass and divisively normalized perceptually processed pixels is highly regular. As in the BRISQUE model [13], paired product coefficients are also extracted at each coordinate by multiplying neighboring MSCN coefficients along four directions: horizontal (H), vertical (V), main-diagonal ($D1$), and secondary-diagonal ($D2$). These

coefficients capture the directional correlation behavior of images, which is also perturbed by the presence of distortions. These coefficients are calculated as follows:

$$\begin{aligned} H(i, j) &= \hat{I}(i, j)\hat{I}(i, j + 1) \\ V(i, j) &= \hat{I}(i, j)\hat{I}(i + 1, j) \\ D1(i, j) &= \hat{I}(i, j)\hat{I}(i + 1, j + 1) \\ D2(i, j) &= \hat{I}(i, j)\hat{I}(i + 1, j - 1) \end{aligned}$$

where $i \in \{1, 2, 3, \dots, M\}$ and $j \in \{1, 2, 3, \dots, N\}$ are spatial indexes.

Histograms of the paired product coefficients show trends similar to those of the MSCN coefficients; wider histograms for noisy images and thinner histograms for blurred images, as depicted in **Fig. 5**. As in the BRISQUE, Asymmetric Generalized Gaussian Distribution (AGGD) is used to model the distributions of the paired product coefficients. The parameters $(\gamma, \beta_l, \beta_r)$ of the AGGD, where γ is the shape parameter and β_l and β_r are the left- and right-half scale parameters, are estimated using a different moment-matching technique [34] that is described in **Appendix B**. The mean of the model distribution is also extracted as a feature:

$$\eta = (\beta_l - \beta_r) \frac{\Gamma(\frac{2}{\gamma})}{\Gamma(\frac{1}{\gamma})} \tag{8}$$

Thus, fitting the AGGD model to each set of paired product coefficients yields four features $(\eta, \gamma, \beta_l, \beta_r)$, which are denoted by pp (acronym for paired products) in **Table 1**. The parameters from the GGD and AGGD fit are obtained at two different scales, although more scales could be used.

The sigma field $\sigma(i, j)$ of a grayscale image given by Eq 7 has also been shown to exhibit a regular structure that is perturbed by the presence of distortion [20]. As in the Feature Maps-Based Referenceless Image Quality Evaluation Engine [20], we extracted three sample statistics (kurtosis, skewness, and arithmetic mean) of the sigma field at three scales to capture the statistical

FIG. 4 Plots of the histograms of MSCN coefficients of pristine and distorted X-ray images. The plot in (a) illustrates the scale-invariant behavior of the MSCN coefficients of undistorted images. Three histograms on the plots in (b) and (c) correspond to the pristine, noisy, and blurred X-ray pictures shown in **Fig. 3**. The terms org, noise, and blur denote original pristine image, noisy image, and image with blur distortion, respectively.

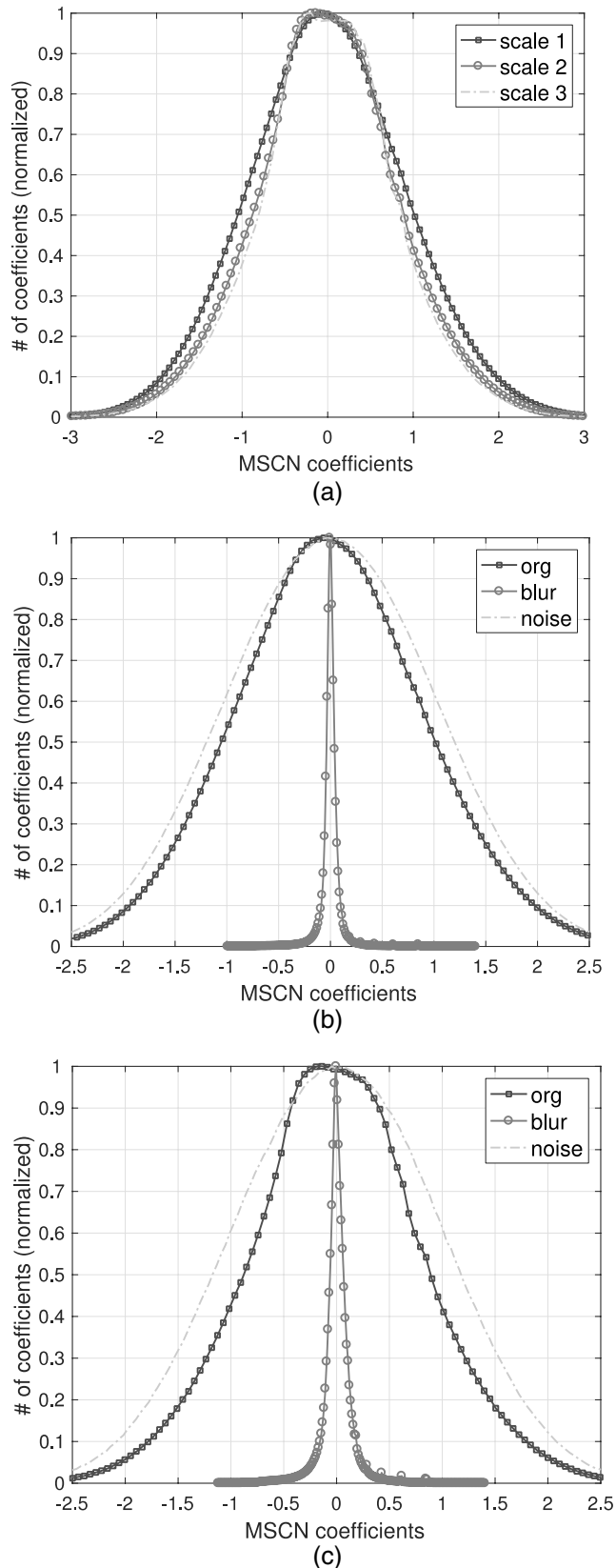


FIG. 5 Plots of the histograms of MSCN diagonal (a), (b) and (c) and horizontal (d), (e) and (f) paired product coefficients of pristine and distorted X-ray images. The plots in (a) and (d) illustrate the scale-invariant behavior of the MSCN paired product coefficients of undistorted image.

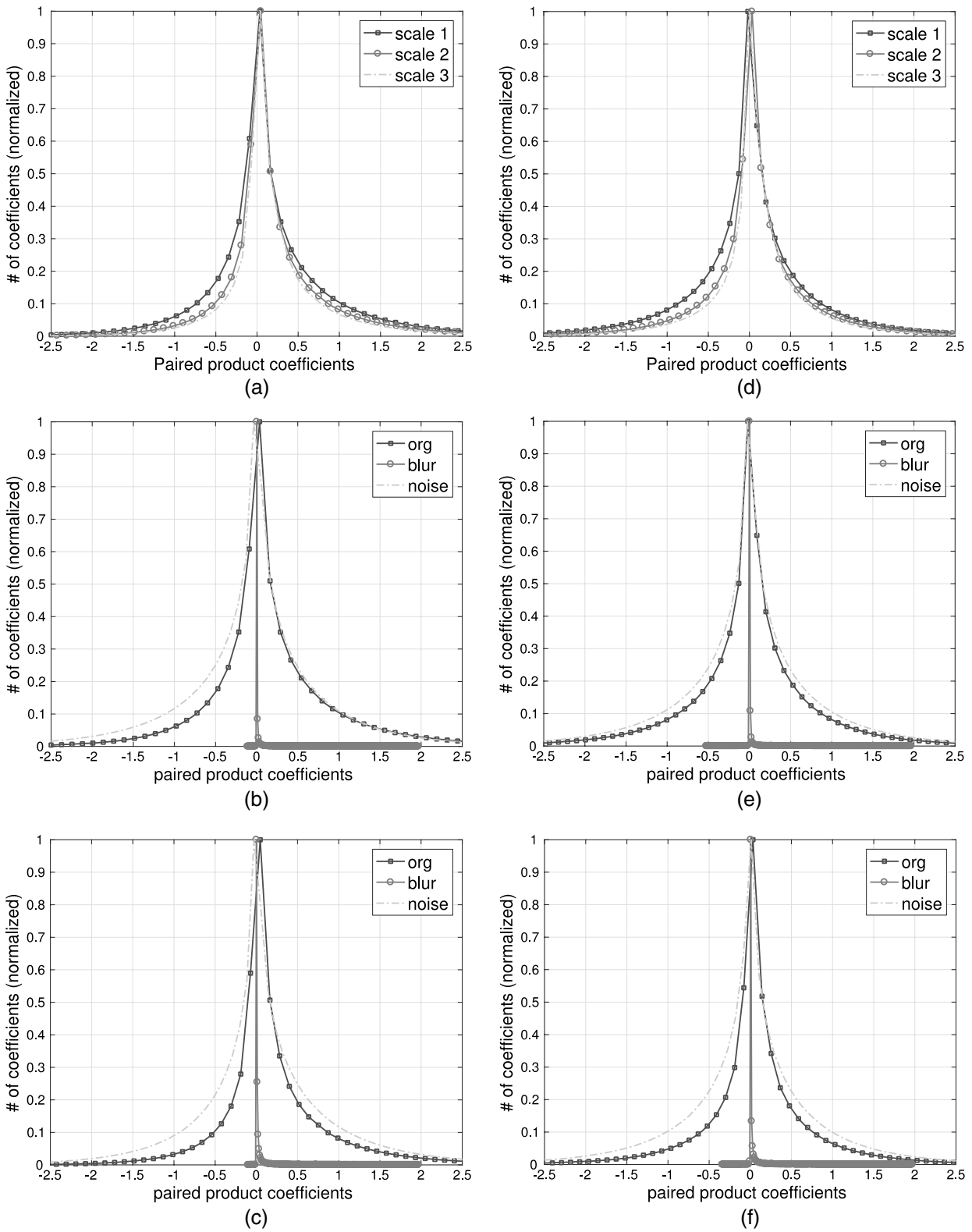


TABLE 1 Feature summary for MSCN(f), pairwise products (pp), and Sigma field (sf) features for the first scale.

Feature ID	Feature Description	Computation Procedure
$f_1 - f_2$	Shape and Variance	Fit GGD to MSCN coefficients
$pp_1 - pp_4$	Shape, mean, left variance, and right variance	Fit AGGD to H pairwise products
$pp_5 - pp_8$	Shape, mean, left variance, and right variance	Fit AGGD to V pairwise products
$pp_9 - pp_{12}$	Shape, mean, left variance, and right variance	Fit AGGD to D1 pairwise products
$pp_{13} - pp_{16}$	Shape, mean, left variance, and right variance	Fit AGGD to D2 pairwise products
$sf_1 - sf_3$	Kurtosis, Skewness, and Mean	Sample statistics of Sigma Field

Note: AGGD = Asymmetric GGD.

regularities (or lack thereof) of natural X-ray images. These features are denoted by sf in **Table 1**.

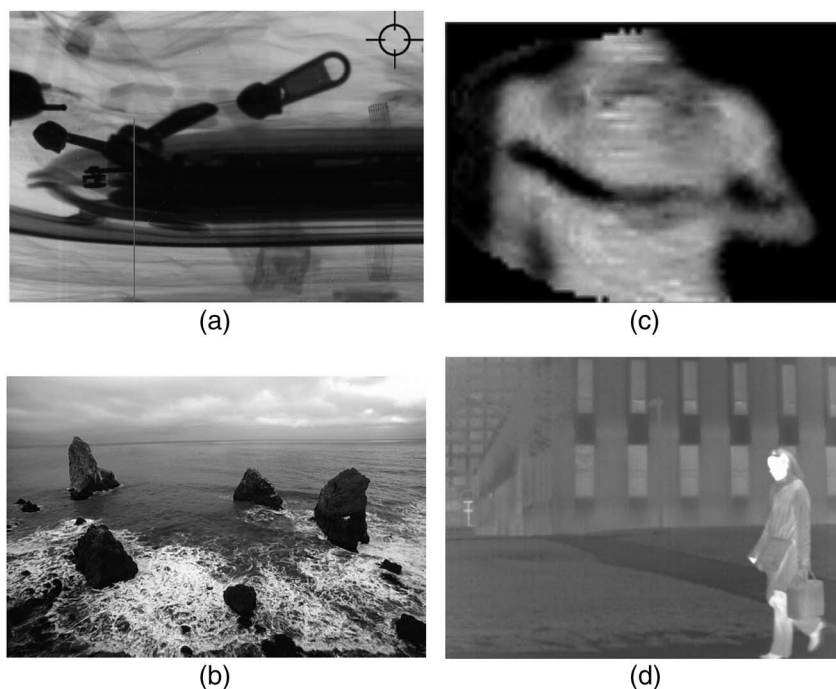
Modality Classifier

In this section, we demonstrate a practical application of the NSS features described above to distinguish different modes of images. Specifically, we developed a Multi-Modality Image Classifier

(MMIC) that effectively classifies an image into one of four given modalities: VL, millimeter-wave (MMW), infrared, and X-ray images. For this test, we use undistorted images from each modality. The reason multiple modalities were selected was to demonstrate the ability of the perceptually relevant NSS descriptors to accurately model the statistics of natural images arising from different imaging modalities. Importantly, while NSS models apply quite well to each of the compared modalities, the models are slightly

FIG. 6

Example image from each modality.

**TABLE 2** Median classification accuracy (with standard deviations) of MMIC across 100 train-test trials for different feature groups.

NSS Feature Set	IR	MMW	VL	X ray	All
MSCN (f)	0.922 ± 0.028	1.000 ± 0.001	0.887 ± 0.048	0.884 ± 0.031	0.913 ± 0.014
Paired products (pp)	0.981 ± 0.014	1.000 ± 0.001	0.952 ± 0.026	0.969 ± 0.016	0.978 ± 0.007
Sigma field (sf)	0.781 ± 0.038	0.940 ± 0.024	0.682 ± 0.050	0.763 ± 0.044	0.780 ± 0.018
$f + pp$	0.981 ± 0.012	1.000 ± 0.001	0.960 ± 0.022	0.973 ± 0.014	0.981 ± 0.006
All combined	0.989 ± 0.012	1.000 ± 0.001	0.971 ± 0.019	0.990 ± 0.010	0.987 ± 0.005

different. Indeed, these differences can be used to efficiently distinguish them.

A total of 2,000 images were obtained from different sources: 387 pristine VL images from the BSD [35] and LIVE [36] databases; 505 IR images from the MORRIS [37], KASER [38], and NIST [39] databases by random selection; 531 MMW frames extracted from 13 videos provided by NIST; and 577 X-ray images obtained from the GDXray [25] and NIST databases by random selection. An example image from each modality is shown in Fig. 6. Since the images were obtained from highly diverse sources, there was considerable intraclass variation in the size, quality, resolution, and dynamic range of the images. After extracting NSS features as described earlier, a supervised classifier was taught on the training data. We trained a Support Vector Classifier with the radial basis function (RBF) kernel against the ground truth label of each image in the training set. To test the performance of the MMIC, we computed results over 100 iterations of randomly sampled train and test sets and reported median results. At each iteration, we randomly split the image data into two disjoint 80 % train and 20 % test sets. Median accuracies from 100 train/test splits for various feature sets are reported in Table 2.

It may be observed from Table 2 that BRISQUE features (f and pp) delivered higher classification accuracy than the sigma field features over all modalities. In particular, paired product (pp) features were significantly more discriminative than the other feature sets, since VL, IR, MMW, and X-ray images all have different degrees of spatial correlation induced by resolution limitations and also contain different degrees of detail, which is efficiently captured by the statistics of products of neighboring pixels. There was a slight improvement in accuracy by combining features from both NSS models. In order to visualize which modalities are easily confused, we plotted the confusion matrix for each modality in Fig. 7. It is worth noting that a small percentage of VL images were misclassified as X-ray images. These cases mainly

FIG. 7 Confusion matrix with rows as true class and columns as predicted class show the mean classification accuracy of the MMIC classifier.

	IR	MMW	VL	X-ray
IR	0.991	0.000	0.009	0.000
MMW	0.000	1.000	0.000	0.000
VL	0.000	0.000	0.958	0.042
X-ray	0.009	0.000	0.000	0.991

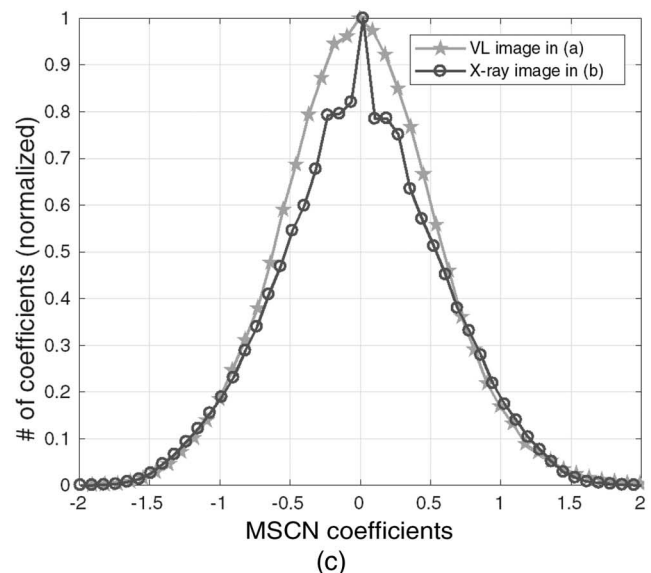
FIG. 8 An example of a pristine VL image with an out-of-focus background misclassified as an X-ray image by the MMIC classifier, along with a comparison of the histogram of their MSCN coefficients.



(a)



(b)



(c)

correspond to VL images that have a shallow depth of field resulting in an out-of-focus background, making them exhibit statistically similar properties as X-ray images (as shown in Fig. 8), which generally possess fewer high-frequency components. The classification results reported in Table 2 show that NSS models can be used to efficiently discriminate between different modes of images. Since MMIC follows a modular approach in the number of different modalities it can handle, it should be possible to test it on an even larger set of unique modality types, depending on the ones used for training.

Conclusions

We found that NSS models apply quite well to X-ray images. They capture the statistical consistencies of X-ray images as effectively as they do with VL images. Furthermore, the NSS of X-ray images can be used to automatically distinguish them from images from other modalities. We believe that these perceptually powerful NSS features will prove to be very useful for describing and measuring the loss of statistical consistency of distorted images. Going forward, we plan to apply our NSS image-modeling paradigm to the important problem of perceptual assessment of X-ray image quality and to develop training-free X-ray image-quality predictors that can accurately predict the perceptual quality of X-ray images and, in particular, their effect of distortion on the human visual task performance.

ACKNOWLEDGMENTS

The authors thank NIST for providing their pristine X-ray and IR images.

Appendix A

The GGD [33] is given by the following equation:

$$f(x; \alpha, \sigma_{ggd}^2) = \frac{\alpha}{2\beta\Gamma(1/\alpha)} \exp\left(-\left(\frac{|x|}{\beta}\right)^\alpha\right) \tag{A1}$$

where

$$\beta = \sigma_{ggd} \sqrt{\frac{\Gamma(1/\alpha)}{\Gamma(3/\alpha)}} \tag{A2}$$

and $\Gamma(\cdot)$ is the gamma function:

$$\Gamma(a) = \int_0^\infty t^{a-1} e^{-t} dt \quad a > 0. \tag{A3}$$

the above expression, α is the shape parameter while σ_{ggd}^2 determines the variance of the distribution. Now we describe the moment-matching technique used in Ref. [33] to estimate the GGD parameters.

- (1) The sample variance of the zero-mean MSCN coefficients is first estimated as $\hat{\sigma}_{ggd}^2 = \frac{1}{N} \sum_{i=1}^N x_i^2$.
- (2) Next, the ratio $\rho = \hat{\sigma}_{ggd}^2 / \hat{E}^2[|X|]$ is computed, where $\hat{E}[|X|] = \frac{1}{N} \sum_{i=1}^N |x_i|$.
- (3) A lookup table for generalized Gaussian ratio function, $r(\alpha)$, is designed for $0 < \alpha < 2$, where $r(\alpha) = \frac{\Gamma(1/\alpha)\Gamma(1/\alpha)}{\Gamma^2(2/\alpha)}$.
- (4) Finally, the shape parameter is estimated by finding a solution to $\hat{\alpha} = r^{-1}(\rho)$ via a lookup table. $(\hat{\alpha}, \hat{\sigma}_{ggd})$ are the final estimated shape parameters of the GGD distribution obtained using a simple but effective moment-matching approach.

Appendix B

The AGGD [34] is given by the following:

$$f(x; \gamma, \beta_l, \beta_r) = \begin{cases} \frac{\gamma}{(\beta_l + \beta_r)\Gamma(\frac{\gamma}{\beta_l})} \exp\left(-\left(\frac{x}{\beta_l}\right)^\gamma\right) & x < 0 \\ \frac{\gamma}{(\beta_l + \beta_r)\Gamma(\frac{\gamma}{\beta_r})} \exp\left(-\left(\frac{x}{\beta_r}\right)^\gamma\right) & x \geq 0 \end{cases} \tag{A4}$$

where β_l and β_r are given by Eq A5:

$$\beta_l = \sigma_l \sqrt{\frac{\Gamma(1/\gamma)}{\Gamma(3/\gamma)}}, \quad \beta_r = \sigma_r \sqrt{\frac{\Gamma(1/\gamma)}{\Gamma(3/\gamma)}} \tag{A5}$$

In the above expression, γ is the shape parameter while β_l and β_r are the left- and right-half scale parameters of the distribution. The parameters $(\gamma, \beta_l, \beta_r)$ of the AGGD are estimated using a moment-matching technique described in Ref. [34].

- (1) The ratio $\hat{R} = \hat{r} \frac{(\hat{\eta}^3 + 1)(\hat{\eta} + 1)}{(\hat{\eta}^2 + 1)^2}$ is computed, where an unbiased estimate of r is $\hat{r} = \frac{(\sum |x_k|)^2}{\sum x_k^2}$, and η is $\hat{\eta} = \frac{\sqrt{\frac{1}{N_l} \sum_{k=1, x_k < 0}^N x_k^2}}{\sqrt{\frac{1}{N_r} \sum_{k=1, x_k \geq 0}^N x_k^2}}$.
- (2) A lookup table for inverse generalized Gaussian ratio function, $\rho(\eta)$, is designed for $0 < \eta < 2$, where $\rho(\eta) = \frac{\Gamma^2(2/\eta)}{\Gamma(1/\eta)\Gamma(1/\eta)}$.
- (3) The shape parameter is estimated by finding a solution to $\hat{\gamma} = \rho^{-1}(\hat{R})$ via a lookup table.
- (4) Finally, the scale parameters, β_l and β_r , are estimated from Eq A5 using the sample estimates of left and right variances, and $\hat{\gamma}$ from Step 3.

References

- [1] Hanke, R., Fuchs, T., and Uhlmann, N., "X-ray Based Methods for Non-destructive Testing and Material Characterization," *Nucl. Instrum. Methods Phys. Res., Sect. A*, Vol. 591, No. 1, 2008, pp. 14–18, <https://doi.org/10.1016/j.nima.2008.03.016>
- [2] Deschler-Erb, E., Lehmann, L., Pernet, L., Vontobel, P., and Hartmann, S., "The Complementary Use of Neutrons and X-Rays for the Non-destructive Investigation of

- Archaeological Objects from Swiss Collections,” *Archaeometry*, Vol. 46, No. 4, 2004, pp. 647–661, <https://doi.org/10.1111/j.1475-4754.2004.00180.x>
- [3] Haff, R. P. and Toyofuku, N., “X-ray Detection of Defects and Contaminants in the Food Industry,” *Sens. Instrum. Food Qual. Saf.*, Vol. 2, No. 4, 2008, pp. 262–273, <https://doi.org/10.1007/s11694-008-9059-8>
- [4] Pfeiffer, F., Weitkamp, T., Bunk, O., and David, C., “Phase Retrieval and Differential Phase-Contrast Imaging with Low-Brilliance X-ray Sources,” *Nat. Phys.*, Vol. 2, No. 4, 2006, pp. 258–261, <https://doi.org/10.1038/nphys265>
- [5] Arfelli, F., Assante, M., Bonvicini, V., Bravin, A., Cantatore, G., Castelli, E., Dalla Palma, L., Di Michiel, M., Longo, R., Olivo, A., Pani, S., Pontoni, D., Poropat, P., Prest, M., Rashevsky, A., Tromba, G., Vacchi, A., Vallazza, E., and Zanconati, F., “Low-Dose Phase Contrast X-ray Medical Imaging,” *Phys. Med. Biol.*, Vol. 43, No. 10, 1998, p. 2845, <https://doi.org/10.1088/0031-9155/43/10/013>
- [6] Zentai, G., “X-ray Imaging for Homeland Security,” *Int. J. Signal Imag. Syst. Eng.*, Vol. 3, No. 1, 2010, pp. 13–20, <https://doi.org/10.1504/IJSISE.2010.034628>
- [7] Singh, S. and Singh, M., “Explosives Detection Systems (EDS) for Aviation Security,” *Signal Process.*, Vol. 83, No. 1, 2003, pp. 31–55, [https://doi.org/10.1016/S0165-1684\(02\)00391-2](https://doi.org/10.1016/S0165-1684(02)00391-2)
- [8] Marshall, M. and Oxley, J. C., *Aspects of Explosives Detection*, Elsevier, Oxford, United Kingdom, 2011, 302p.
- [9] ANSI-N42.47-2010, *American National Standard for Measuring the Imaging Performance of X-ray and Gamma-Ray Systems for Security Screening of Humans*, IEEE, Piscataway, NJ, 2010, www.ieee.org
- [10] ANSI-N42.55-2013, *American National Standard for the Performance of Portable Transmission X-ray Systems for Use in Improvised Explosive Device and hazardous Device Detection*, IEEE, Piscataway, NJ, 2013, www.ieee.org
- [11] Chen, F., Pan, J., and Han, Y., “An Effective Image Quality Evaluation Method of X-ray Imaging System,” *J. Comput. Inform. Syst.*, Vol. 7, No. 4, 2011, pp. 1278–1285, http://web.archive.org/web/20180426161523/https://www.researchgate.net/publication/267363706_An_Effective_Image_Quality_Evaluation_Method_of_X-Ray_Imaging_System (accessed 20 April 2018).
- [12] Bolfig, A., Halbherr, T., and Schwaninger, A., “How Image Based Factors and Human Factors Contribute to Threat Detection Performance in X-ray Aviation Security Screening,” presented at the *Symposium of the Austrian HCI and Usability Engineering Group*, Graz, Austria, Nov. 20–21, 2008, Springer-Verlag, Berlin, Germany, pp. 419–438.
- [13] Mittal, A., Moorthy, A. K., and Bovik, A. C., “No-Reference Image Quality Assessment in the Spatial Domain,” *IEEE Trans. Image Process.*, Vol. 21, No. 12, 2012, pp. 4695–4708, <https://doi.org/10.1109/TIP.2012.2214050>
- [14] Moorthy, A. K. and Bovik, A. C., “Blind Image Quality Assessment: From Natural Scene Statistics to Perceptual Quality,” *IEEE Trans. Image Process.*, Vol. 20, No. 12, 2011, pp. 3350–3364, <https://doi.org/10.1109/TIP.2011.2147325>
- [15] Olshausen, B. A. and Field, D. J., “Emergence of Simple-Cell Receptive Field Properties by Learning a Sparse Code for Natural Images,” *Nature*, Vol. 381, No. 6583, 1996, pp. 607–609, <https://doi.org/10.1038/381607a0>
- [16] Ruderman, D. L., “The Statistics of Natural Images,” *Network Comput. Neural Syst.*, Vol. 5, No. 4, 1994, pp. 517–548, https://doi.org/10.1088/0954-898X_5_4_006
- [17] Simoncelli, E. P. and Olshausen, B. A., “Natural Image Statistics and Neural Representation,” *Ann. Rev. Neurosci.*, Vol. 24, No. 1, 2001, pp. 1193–1216, <https://doi.org/10.1146/annurev.neuro.24.1.1193>
- [18] Olshausen, B. A. and Field, D. J., “Natural Image Statistics and Efficient Coding,” *Network Comput. Neural Syst.*, Vol. 7, No. 2, 1996, pp. 333–339, <https://doi.org/10.1088/0954-898X/7/2/014>
- [19] Saad, M. A., Bovik, A. C., and Charrier, C., “Blind Image Quality Assessment: A Natural Scene Statistics Approach in the DCT Domain,” *IEEE Trans. Image Process.*, Vol. 21, No. 8, 2012, pp. 3339–3352, <https://doi.org/10.1109/TIP.2012.2191563>
- [20] Ghadiyaram, D. and Bovik, A. C., “Feature Maps Driven No-Reference Image Quality Prediction of Authentically Distorted Images,” *Human Vision and Electronic Imaging XX*, International Society for Optics and Photonics, Bellingham, WA, 2015, 93940J.
- [21] Goodall, T. R., Bovik, A. C., and Paulter, N. G., “Tasking on Natural Statistics of Infrared Images,” *IEEE Trans. Image Process.*, Vol. 25, No. 1, 2016, pp. 65–79, <https://doi.org/10.1109/TIP.2015.2496289>
- [22] Moreno-Villamarn, D. E., Bentez-Restrepo, H. D., and Bovik, A. C., “Predicting the Quality of Fused Long Wave Infrared and Visible Light Images,” *IEEE Trans. Image Process.*, Vol. 26, No. 7, 2017, pp. 3479–3491, <https://doi.org/10.1109/TIP.2017.2695898>
- [23] Smeulders, A. W., Worring, M., Santini, S., Gupta, A., and Jain, R., “Content-Based Image Retrieval at the End of the Early Years,” *IEEE Trans. Pattern Anal. Mach. Intell.*, Vol. 22, No. 12, 2000, pp. 1349–1380, <https://doi.org/10.1109/34.895972>
- [24] Müller, H., Michoux, N., Bandon, D., and Geissbuhler, A., “A Review of Content-Based Image Retrieval Systems in Medical Applications—Clinical Benefits and Future Directions,” *Int. J. Med. Inform.*, Vol. 73, No. 1, 2004, pp. 1–23, <https://doi.org/10.1016/j.ijmedinf.2003.11.024>
- [25] Mery, D., Riffo, V., Zscherpel, U., Mondragón, G., Lillo, I., Zuccar, I., Lobel, H., and Carrasco, M., “GDxray: The Database of X-ray Images for Nondestructive Testing,” *J. Nondestr. Eval.*, Vol. 34, No. 4, 2015, 42, <https://doi.org/10.1007/s10921-015-0315-7>
- [26] Hasinoff, S. W., “Photon, Poisson Noise,” *Computer Vision: A Reference Guide*, Springer, Boston, MA, 2014, pp. 608–610.
- [27] Heintzmann, R., Relich, P. K., Nieuwenhuizen, R. P., Lidke, K. A., and Rieger, B., “Calibrating Photon Counts from a Single Image,” *arXiv preprint arXiv:1611.05654*, 2016, <https://web.archive.org/web/20180420035554/https://arxiv.org/pdf/1611.05654.pdf> (accessed 20 April 2018).
- [28] van Vliet, L. J., Sudar, D., and Young, I. T., “Digital Fluorescence Imaging Using Cooled CCD Array Cameras Invisible,” *Cell Biology*, 2nd ed., Vol. 3, J. E. Celis, Ed., Academic Press, New York, 1998, pp. 109–120, https://web.archive.org/web/20180420040622/https://qi.tnw.tudelft.nl/fileadmin/Faculteit/TNW/Over_de_faculteit/Afdelingen/Imaging_Science_and_Technology/Research/Research_Groups/Quantitative_Imaging/Publications/List_Publications/doc/AP98LVDSTY.pdf (accessed 20 April 2018).

- [29] Liu, C., Szeliski, R., Kang, S. B., Zitnick, C. L., and Freeman, W. T., "Automatic Estimation and Removal of Noise from a Single Image," *IEEE Trans. Pattern Anal. Mach. Intell.*, Vol. 30, No. 2, 2008, pp. 299–314, <https://doi.org/10.1109/TPAMI.2007.1176>
- [30] Foi, A., Trimeche, M., Katkovnik, V., and Egiazarian, K., "Practical Poissonian-Gaussian Noise Modeling and Fitting for Single-Image Raw-Data," *IEEE Trans. Image Process.*, Vol. 17, No. 10, 2008, pp. 1737–1754, <https://doi.org/10.1109/TIP.2008.2001399>
- [31] Mittal, A., Soundararajan, R., and Bovik, A. C., "Making a 'Completely Blind' Image Quality Analyzer," *IEEE Signal Process. Lett.*, Vol. 20, No. 3, 2013, pp. 209–212, <https://doi.org/10.1109/LSP.2012.2227726>
- [32] Bovik, A. C., "Automatic Prediction of Perceptual Image and Video Quality," *Proc. IEEE*, Vol. 101, No. 9, 2013, pp. 2008–2024.
- [33] Sharifi, K. and Leon-Garcia, A., "Estimation of Shape Parameter for Generalized Gaussian Distributions in Subband Decompositions of Video," *IEEE Trans. Circuits Syst. Video Technol.*, Vol. 5, No. 1, 1995, pp. 52–56, <https://doi.org/10.1109/76.350779>
- [34] Lasmar, N.-E., Stitou, Y., and Berthoumieu, Y., "Multiscale Skewed Heavy Tailed Model for Texture Analysis," presented at the *2009 16th IEEE International Conference on Image Processing (ICIP)*, Cairo, Egypt, Nov. 7–10, 2009, IEEE, Piscataway, NJ, pp. 2281–2284.
- [35] Martin, D., Fowlkes, C., Tal, D., and Malik, J., "A Database of Human Segmented Natural Images and Its Application to Evaluating Segmentation Algorithms and Measuring Ecological Statistics," presented at the *Eighth International Conference on Computer Vision*, July 7–14, 2001, Vancouver, Canada, IEEE, Piscataway, NJ, pp. 416–423.
- [36] Sheikh, H. R., Wang, Z., Cormack, L., and Bovik, A. C., "Live Image Quality Assessment Database Release 2," 2005.
- [37] Morris, N. J., Avidan, S., Matusik, W., and Pfister, H., "Statistics of Infrared Images," presented at the *2007 IEEE Conference on Computer Vision and Pattern Recognition*, Minneapolis, MN, June 17–22, 2007, IEEE, Piscataway, NJ, pp. 1–7.
- [38] Kaser, J. Y., "Utilizing Natural Scene Statistics and Blind Image Quality Analysis of Infrared Imagery," M.S. thesis, The University of Texas at Austin, Austin, TX, 2013.
- [39] Rowe, J. L., *The Impact of Thermal Imaging Camera Display Quality on Fire Fighter Task Performance*, National Institute of Standards and Technology, Gaithersburg, MD, 2008, 154p.